Applied Catalysis B: Environmental 243 (2019) 27–35

Contents lists available at ScienceDirect

Applied Catalysis B: Environmental

journal homepage: www.elsevier.com/locate/apcatb

A New and stable Mo-Mo_2C modified g-C_3N_4 photocatalyst for efficient visible light photocatalytic H_2 production

Jie Dong[a], Ying Shi[a], Cunping Huang[b], Qiang Wu[a,*], Tao Zeng[c,*], Weifeng Yao[a,d,*]

[a] Shanghai Key Laboratory of Materials Protection and Advanced Materials in Electric Power, College of Environmental & Chemical Engineering, Shanghai University of Electric Power, Shanghai, PR China

[b] Aviation Fuels Research Laboratory, Federal Aviation Administration William J. Hughes Technical Center, Atlantic City International Airport, Atlantic City, NJ 08405, United States

[c] Shanghai Key Laboratory of Engineering Materials Application and Evaluation, Shanghai Research Institute of Materials, Shanghai 200437, PR China

[d] Shanghai Institute of Pollution Control and Ecological Security, Shanghai, PR China

ARTICLE INFO

Keywords:
Noble-metal-free cocatalyst
Hydrogen production
Mo_2C
Photocatalysis

ABSTRACT

Design and preparation of highly efficient and stable cocatalysts are critical to the improvement of photocatalyst performance. A traditional cocatalyst consists of metal nanoparticles for the separation of photo-induced electron-hole pairs and for the reduction of protons. In this research we report a metal-semiconductor composite cocatalyst to increase light adsorption and to effectively enhance proton reduction capacity. A molybdenum rich molybdenum carbide (Mo-Mo_2C) based noble-metal-free metal/semiconductor cocatalyst was loaded onto graphitic carbon nitride (g-C_3N_4) for highly efficient photocatalytic H_2 evolution from water. The Mo-Mo_2C was synthesized via a temperature-programmed reaction using $(NH_4)_6Mo_7O_{24}{\cdot}4H_2O$ as a precursor. The cocatalyst loaded 2.0 wt.% Mo-Mo_2C/g-C_3N_4 composite photocatalyst has demonstrated excellent photocatalytic performance. The hydrogen evolution rate for the 2.0 wt.% Mo-Mo_2C/g-C_3N_4 nanocomposites can be as high as 219.7 μmol h^{-1} g^{-1}, which is 440 times higher than that of g-C_3N_4 alone and 90% as high as 0.5 wt.% Pt/g-C_3N_4 photocatalyst (244.1 μmol h^{-1} g^{-1}). Due to strong synergetic effects between Mo and Mo_2C nanoparticles, this rate is 11.47 and 3.60 times higher than those for 2.0 wt.% Mo/g-C_3N_4 (19.1 μmol h^{-1} g^{-1}) and 2.0 wt.% Mo_2C/g-C_3N_4 (60.9 μmol h^{-1} g^{-1}) photocatalysts respectively. Moreover, the 2.0 wt.% Mo-Mo_2C/g-C_3N_4 catalyst is significantly stable for application in photocatalytic hydrogen evolution, with an apparent quantum efficiency of 8.3%—one of the highest noble-metal-free efficiencies reported in literature. All results indicate that metal/semiconductor composites can serve as highly efficient cocatalysts for photocatalytic hydrogen evolution from water reduction.

1. Introduction

In the past few decades increasing energy demands have resulted in greater consumption of fossil fuels, creating environmental concerns and, in turn, greatly invigorated efforts into the research and development of alternate renewable energy sources [1–3]. Solar photocatalytic water splitting for the production of hydrogen is one of the promising processes for the production of eco-friendly renewable energy [4–6]. In order to efficiently convert solar energy to hydrogen chemical energy a photocatalyst is necessary. To be highly effective a photocatalyst must absorb as broad a sunlight spectrum as possible [7].

Among the robust and visible-light-driven photocatalysts, graphitic carbon nitride (g-C_3N_4) has been widely accepted as a next generation photocatalyst due to its remarkable physicochemical stability and attractive electronic band structures [8–11]. g-C_3N_4 can be synthesized via a facile thermal polymerization of less expensive precursors such as urea [12–14], cyanamide [15–18], dicyandiamide [19–21], thiourea [22–24] and melamine [25,26]. Recently, Wang et al. reported for the first time that g-C_3N_4 can be used to generate hydrogen via water splitting under visible light irradiation, even in the absence of a noble metal cocatalyst [4]. However, owing to the high recombination rate of photo-generated charge carriers, low electrical conductivity and narrow absorption range (< 460 nm), pristine g-C_3N_4 does not have a very high level of photocatalytic activity [27].

A cocatalyst is crucial for the separation of photo-induced electron-hole pairs and the reduction of protons in order to increase the

* Corresponding authors at: Shanghai Key Laboratory of Materials Protection and Advanced Materials in Electric Power, College of Environmental & Chemical Engineering, Shanghai University of Electric Power, Shanghai, PR China.

E-mail addresses: qiangwu@shiep.edu.cn (Q. Wu), zengtao@srim.com.cn (T. Zeng), yaoweifeng@shiep.edu.cn (W. Yao).

https://doi.org/10.1016/j.apcatb.2018.10.016
Received 22 July 2018; Received in revised form 2 October 2018; Accepted 7 October 2018
Available online 09 October 2018
0926-3373/ © 2018 Elsevier B.V. All rights reserved.

efficiency of a photocatalyst [28–30]. Normally, cocatalysts for H_2 production consist mainly of noble metals such as platinum [31], palladium [32], rhodium [33] or gold [34], but the application of these noble metals is limited due to high costs and scarcity. Thus, the exploitation of inexpensive and earth-abundant alternative cocatalysts is of great significance.

Mo_2C has recently attracted intensive research interest as a promising electrocatalyst for hydrogen evolution reaction (HER) at significant low cost due to its Pt-like electronic structures and electrocatalytic activities for HER [35–38]. Our group has more recently reported a facile method for the synthesis of a metallic Mo rich Mo_2C (Mo-Mo_2C) electrocatalyst with an enhanced electrocatalytic activity toward HER [35], since metallic Mo can improve the electron conductivity of Mo_2C. However, to the best of our knowledge, Mo-Mo_2C has not been reported as a cocatalyst for photocatalytic H_2 production from water reduction.

Our previous research into the Ag rich Ag_3PO_4 photocatalyst [39] determined that additional metal particles in a semiconductor can effectively increase the photocatalytic activity of the photocatalyst. We have also found that a highly effective electrocatalyst toward HER can be a highly efficient cocatalyst for photocatalytic hydrogen production as well [40–42]. In this research we report, for the first time, a highly active noble-metal-free Mo-Mo_2C cocatalyst on g-C_3N_4 for photocatalytic H_2 production under visible light irradiation. This metal-semiconductor cocatalyst can absorb a wider spectrum of solar irradiation and can reduce the recombination rate of electron-hole pairs more significantly, leading to higher quantum efficiency for solar energy conversion.

2. Experimental

All reagents used in this research were commercially available, without need for further purification.

2.1. Synthesis of Mo-Mo_2C cocatalyst

The synthesis of Mo-Mo_2C is adopted from a published method [35]. In a typical process, 2.0 mmol $(NH_4)_6Mo_7O_{24}{\cdot}4H_2O$ and 36.0 mmol aniline were added into a 100 mL 3-necked round-bottom flask containing 40 mL of deionized water. Next, 1.0 M HCl aqueous solution was added to adjust the solution pH to 4.0. After reaction at 50 °C for 4 h the precipitates were collected via centrifuging and thoroughly washed with deionized water and ethanol. A white powder, $Mo_3O_{10}(C_6H_8N)_2{\cdot}2H_2O$, was obtained after drying overnight in a vacuum oven at 60 °C. Next the $Mo_3O_{10}(C_6H_8N)_2{\cdot}2H_2O$ product was transferred into a tube furnace. Under vacuum the furnace tube was filled with Ar gas. The sample was heated from room temperature to 775 °C at a heating rate of 2 °C/min and annealed at 775 °C for 2 h. The Mo-Mo_2C sample was obtained after naturally cooling the furnace to room temperature. Pure Mo_2C was also synthesized using the same procedures, except that the targeted annealing temperature was controlled at 675 °C.

2.2. Synthesis of g-C_3N_4 photocatalyst

Graphitic carbon nitride (g-C_3N_4) was synthesized as follows: 5.00 g melamine was transferred into a quartz crucible that was placed in a muffle furnace. The furnace was first heated from room temperature to 500 °C at a 2 °C/min heating rate. After 2 h the sample temperature was increased from 500 °C to 520 °C at the same heating rate and the temperature was maintained at 520 °C for 2 h. Next, the bulk g-C_3N_4 sample was rapidly cooled to room temperature. Finally, the bulk g-C_3N_4 sample was ground into powder and preserved in a glass bottle.

2.3. Preparation of Mo-Mo_2C/g-C_3N_4 photocatalysts

Mo-Mo_2C/g-C_3N_4 photocatalysts were prepared using an ultrasound assisted deposition method [43]. In a typical procedure a certain amount of prepared g-C_3N_4 powder was added into a beaker containing 25 mL methanol. After sonication for 30 min the Mo-Mo_2C nanorod sample was dispersed in the prepared suspension and stirred at room temperature for 24 h. The remaining methanol was removed by evaporation under a nitrogen gas stream. The obtained yellowish powder was collected and dried overnight in a vacuum oven at 60 °C. The Mo_2C/g-C_3N_4 catalyst sample was synthesized using the same procedure, with Mo_2C as the cocatalyst. The Mo/g-C_3N_4 catalyst sample was synthesized using the photodeposition method. All the loading weight percent of Mo-Mo_2C, Mo_2C and Mo was 2.0 wt.% based on the total cocatalyst and g-C_3N_4 mass. X-Ray photoelectron spectrometer (XPS) and Inductively coupled plasma (ICP) analyses show that the Mo-Mo_2C concentration in as-synthesized 2.0 wt% Mo-Mo_2C/g-C_3N_4 is 1.60 wt.% and 1.34 wt.%, respectively (Table S1). Considering the experimental errors, these results are close to the apparent 2.0 wt.% loading amount. In this research, we use apparent 2.0 wt.% as Mo-Mo_2C loading concentration for Mo-Mo_2C/g-C_3N_4 photocatalyst.

2.4. Photocatalyst characterizations

Transmission electron microscope (TEM) images were obtained on a JEM-2010 and FEI Tecnai G2 F30 electron microscope operated at 200 kV. Powder X-ray diffraction (XRD) patterns were recorded with a Bruker-D8 X-ray diffractometer equipped with Cu Kα radiation. Raman spectra are recorded on a laser confocal Raman microspectrometer (inVia) with an excitation laser wavelength of 532 nm. The field emission scanning electronic microscopy (FESEM) images were collected with a Hitachi SU-1500 SEM system at 5 kV. Fourier transform infrared spectroscopy (FT-IR) was taken with a Spectrum Two™ FT-IR Spectrometer (PerkinElmer, America). UV–vis diffuse reflectance spectroscopy (DRS) was performed on a UV-2550 spectrophotometer (Shimadzu, Japan) using $BaSO_4$ powder as a reference. X-Ray photoelectron spectrometer (XPS) surveys were conducted with a Thermo ESCALAB 250 Kα spectrometer. The photoluminescence (PL) spectra were measured using the FLS980 Fluorescence Spectrometer (Edinburgh, Britain). The inductively coupled plasma (ICP) measurements were tested by a 710-ES ICP Optical Emission Spectrometer for elemental analysis.

2.5. Evaluation of photocatalyst activities

The photocatalytic activities of photocatalysts were measured using a small flask wrapped in a sheet of tinfoil. The dimensions of the window were 2.0 cm X 2.5 cm. In a typical reaction 5.0 mg Mo-Mo_2C/g-C_3N_4 catalyst powder was added into a 10 mL suspension containing 8 mL H_2O and 2 mL triethanolamine (TEOA) under magnetic stirring. Prior to a photocatalytic reaction, the photolyte suspension was degassed with high purity N_2 gas to remove dissolved oxygen. A 300 W Xe lamp (Perfectlight, China) with a cut off filter ($\lambda > 420$ nm) was used as a visible light source for the photocatalytic hydrogen evolution reaction (HER). The generated H_2 was analyzed using an online gas chromatograph (GC-2014, Shimadzu, Japan; high purity N_2 was used as the carrier gas) equipped with a thermal conductivity detector (TCD). The total amount of H_2 production every hour was recorded as the rate of photocatalytic HER.

The apparent quantum efficiency (AQE) was calculated according to the following equation:

$$\text{Apparent quantum efficiency (\%)} = \frac{\text{The number of reacted electrons}}{\text{The number of incident photons}} \times 100 = \frac{\text{Number of evolved } H_2 \text{ molecules x 2}}{\text{Number of incident photons}} \times 100 = \frac{2 \times n_{H_2}}{I_0 \times t} \times 100$$

where n_{H_2} is the number moles for hydrogen evolution from t = 0 to

time *t*. I_0 ($I_0 = 4.7 \times 10^{-9}$ mol s^{-1}) is the Einstein of incident photons per second measured at λ = 420 nm.

2.6. Photoelectrochemical measurements

Photocurrent measurements, Mott-Schottky (M–S) analyses, electrochemical impedance spectroscopy (EIS) and linear sweep voltammetry (LSV) for photocatalysts were all performed on a CHI660E electrochemical workstation. Working electrodes were prepared as follows: 10.0 mg photocatalysts were dispersed into a mixture containing 450 μL ethanol and 50 μL 5 wt.% Nafion solution and sonicated for at least 30 min to form a homogeneous ink. Next, 25 μL of the ink was coated onto a fluorine doped tin oxide (FTO) glass electrode and dried in air. A saturated calomel electrode (SCE) and a Pt foil were used as reference electrode and counter electrode, respectively. The amperometric i ~ t curves were measured at the 0.2 V potential (vs. SCE) under a 300 W Xe lamp with a 420 nm cut off filter. The M–S plots were recorded at a frequency of 2 kHz in a 0.5 M Na_2SO_4 aqueous solution. LSV spectra were carried out at a 2 mV/s scan rate. EIS tests were measured at an open circuit potential over frequencies ranging from 10^{-2} Hz to 10^6 Hz, with an amplitude of 5 mV. The LSV and EIS were performed in 10 mL of 20% (v/v) TEOA with 40 mL 0.2 M Na_2SO_4 aqueous solution because the electrolyte provides a neutral environment for testing.

3. Results and discussion

3.1. Material characterizations

The Mo-Mo_2C/g-C_3N_4 photocatalyst was prepared in a two-step process. In the first step, the Mo-Mo_2C cocatalyst was synthesized via a temperature-programmed reduction method [35]. Fig. S1 shows the XRD pattern of prepared Mo-Mo_2C. The diffraction peaks of Mo-Mo_2C are fully consistent with those previously reported for Mo-Mo_2C [35]. In the second step, the prepared Mo-Mo_2C powder was loaded onto the surface of a g-C_3N_4 photocatalyst using the ultrasonic assisting deposition method. Fig. 1 illustrates the synthesis scheme of Mo-Mo_2C/g-C_3N_4 photocatalysts. The Mo-Mo_2C/g-C_3N_4 XRD diffraction peaks (Fig. 2) at 13.1° and 27.4° belong to (100) and (002) of g-C_3N_4 [44]. The diffraction peak at 39.4° can be ascribed to the (101) of Mo_2C. FT-IR analysis was carried out in order to further confirm the structure and performance of g-C_3N_4 and Mo-Mo_2C/g-C_3N_4 photocatalysts. The IR peaks (Fig. 3) at 809 and 250 - 1700 cm^{-1} correspond to the tri-s-triazine ring units and stretching modes [44,45]. All these peaks are typically characteristic IR spectra of g-C_3N_4. There are no significant differences between g-C_3N_4 and Mo-Mo_2C/g-C_3N_4 IR spectra. The Raman spectra of bare g-C_3N_4 and 2.0 wt.% Mo-Mo_2C/g-C_3N_4 did not show significant difference in the spectrum either (Fig. S2). These observations indicate that the loading of Mo-Mo_2C cocatalyst particles onto the surface of a g-C_3N_4 photocatalyst does not change the g-C_3N_4 structure.

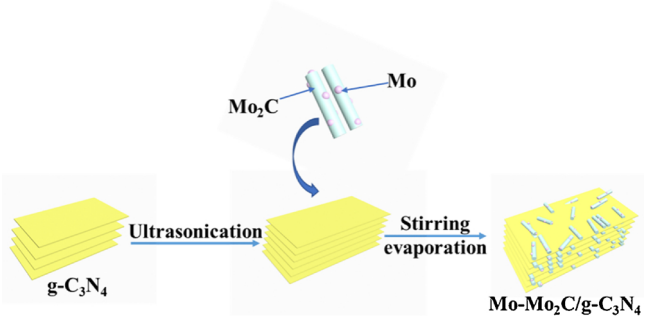

Fig. 1. Schematic illustration of the synthesis procedures of Mo-Mo_2C/g-C_3N_4 photocatalyst.

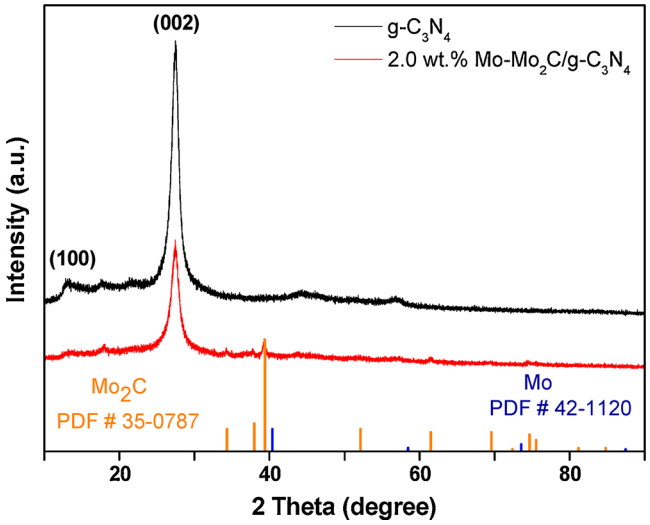

Fig. 2. XRD patterns of g-C_3N_4 and 2.0 wt.% Mo-Mo_2C/g-C_3N_4 photocatalysts.

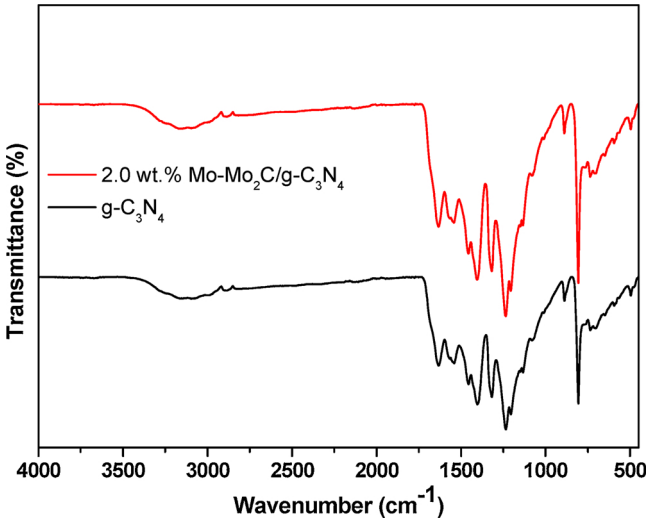

Fig. 3. FT-IR spectra of g-C_3N_4 and 2.0 wt.% Mo-Mo_2C/g-C_3N_4 photocatalysts.

The TEM image (Fig. 4(a)) shows that Mo-Mo_2C cocatalyst crystals consist of nano-belt structures. The lattice fringes of Mo_2C with d-spacings of 0.24 nm and 0.23 nm can be assigned to (002) and (101) crystal planes (Supporting Information, Fig. S3), respectively. The 0.22 nm d-spacing can be ascribed to the (110) crystal plane for a metallic Mo. Fig. 4(b) and (c, d) presents the typical TEM images of bare g-C_3N_4 and 2.0 wt.% Mo-Mo_2C/g-C_3N_4, respectively, where Mo-Mo_2C shows a darker color than g-C_3N_4 in the image. The HRTEM image of Mo-Mo_2C/g-C_3N_4 (Fig. 4e) shows the clear lattice fringes of Mo_2C (d = 0.23 nm and 0.24 nm corresponding to Mo_2C (101) and (002)) coupled with the fringes of g-C_3N_4, implying that two semiconductors contact very tightly. This tight contact enables the stability and promotes the separation and transfer of photogenerated carriers between Mo-Mo_2 and g-C_3N_4. This is definitely beneficial for the photocatalytic hydrogen evolution reaction [46]. The EDS element mapping analysis (Fig. 4(f)) verifies the presence of elemental C, N and Mo in Mo-Mo_2C/g-C_3N_4.

The overall XPS survey spectrum (Fig. 5(a)) suggests the existence of C, N, Mo and O elements, which agrees with the EDS results of Mo-Mo_2C/g-C_3N_4 (Fig. 4(d)). Obviously, there is no Mo element XPS peak in the measured spectrum of bare g-C_3N_4 (Fig. S4). In Fig. 5(b), the C 1 s spectrum shows two binding energy peaks at 288.2 and 284.8 eV, which are associated with sp^2-bonded carbon with nitrogen (N—C═N) [47] and C—C. The N 1 s spectrum is shown in Fig. 5(c). The peaks centered at

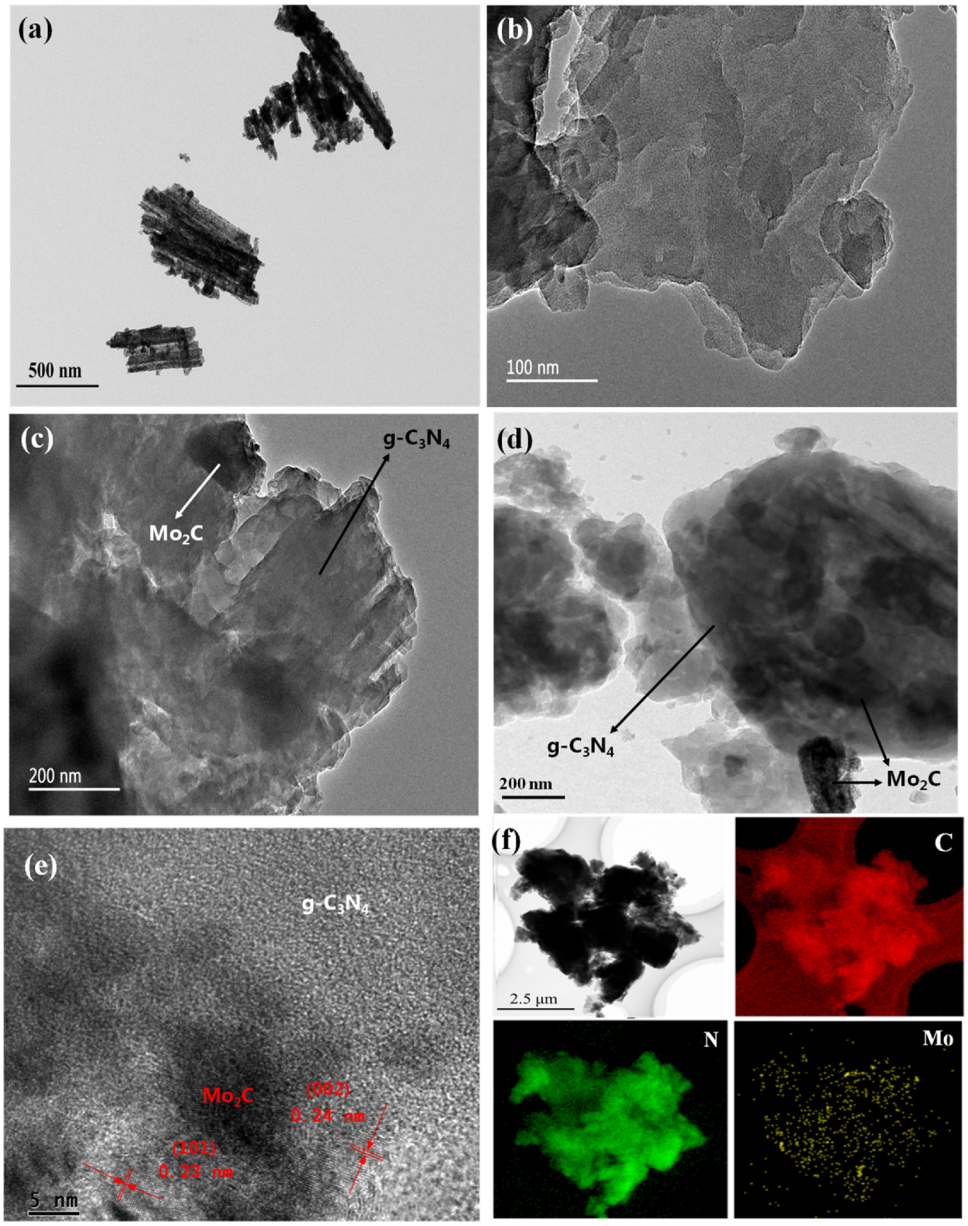

Fig. 4. TEM images of the Mo-Mo_2C (a), g-C_3N_4 (b), 2.0 wt.% Mo-Mo_2C/g-C_3N_4 (c, d), HR-TEM images of the 2.0 wt.% Mo-Mo_2C/g-C_3N_4 (e) and EDS elemental mapping for C, N, Mo elements (f) over the 2.0 wt.% Mo-Mo_2C/g-C_3N_4 photocatalyst.

400.7, 399.3 and 398.6 eV can be attributed to an amino function group with hydrogen (C-NH_2) [48], N-$(R)_3$ [49] and sp^2-hybridized structure in triazine rings (C–N═C) [50]. As shown in Fig. 5(d), the Mo 3d spectrum of Mo-Mo_2C/g-C_3N_4 indicates the existence of +2, +4, +6 and 0 valence states of Mo, showing the coexistence of metallic Mo with Mo_2C. Fig. S5 shows that the Mo 3d and N 1 s XPS spectra of g-C_3N_4, Mo-Mo_2C and 2.0 wt.% Mo-Mo_2C/g-C_3N_4 samples. It is noted that the Mo 3d binding energy of 2.0 wt.% Mo-Mo_2C/g-C_3N_4 exhibits negative-shift trend comparing with that of pristine Mo-Mo_2C (Fig. S5(a)). Meanwhile, the N 1 s binding energy of 2.0 wt.% Mo-Mo_2C/g-C_3N_4 exhibits positive-shift trend comparing with that of g-C_3N_4 (Fig. S5(b)) [51]. These results indicate that the electron density within Mo-Mo_2C increases after deposition of Mo-Mo_2C particles on g-C_3N_4. In other words, when Mo-Mo_2C is deposited on g-C_3N_4, electrons are transferred from g-C_3N_4 to Mo-Mo_2C. This conclusion is supported by the different flat band potentials. The flat band potentials of Mo-Mo_2C and g-C_3N_4 have been determined using Mott-Schottky (M–S) method as -1.03 and -0.47 V vs. SCE, respectively, as introduced in the following section.

3.2. Evaluation of optical properties of 2.0 wt.% Mo-Mo_2C/g-C_3N_4 photocatalyst

The UV–vis diffuse reflectance spectroscopy (DRS) of Mo-Mo_2C, pure g-C_3N_4 and 2.0 wt.% Mo-Mo_2C/g-C_3N_4 cocatalyst and photocatalysts are shown in Fig. 6(a). Compared with pure g-C_3N_4 UV–vis DRS, the UV–vis DRS of 2.0 wt.% Mo-Mo_2C/g-C_3N_4 shows an enhanced photo-absorption in the wavelength range from 400 to 800 nm that is caused by the strong photo-absorption of Mo-Mo_2C cocatalyst. In addition, Mo-Mo_2C demonstrates stronger photo-absorption in the wavelength ranging from 200 to 800 nm. Fig. 6(b) and (c) show the Tauc plot of $(\alpha h\nu)^2$ as a function of photonic energy ($h\nu$) for g-C_3N_4 and Mo-Mo_2C, respectively. The Tauc functions are derived using the Kubelka-Munk method [52]. The corresponding band gap energies calculated based on Tauc plots are 2.71 eV and 1.49 eV for g-C_3N_4 and Mo-Mo_2C, respectively.

A photoluminescence (PL) spectrum is commonly used to evaluate the charge separation efficiency of photogenerated electron-hole pairs.

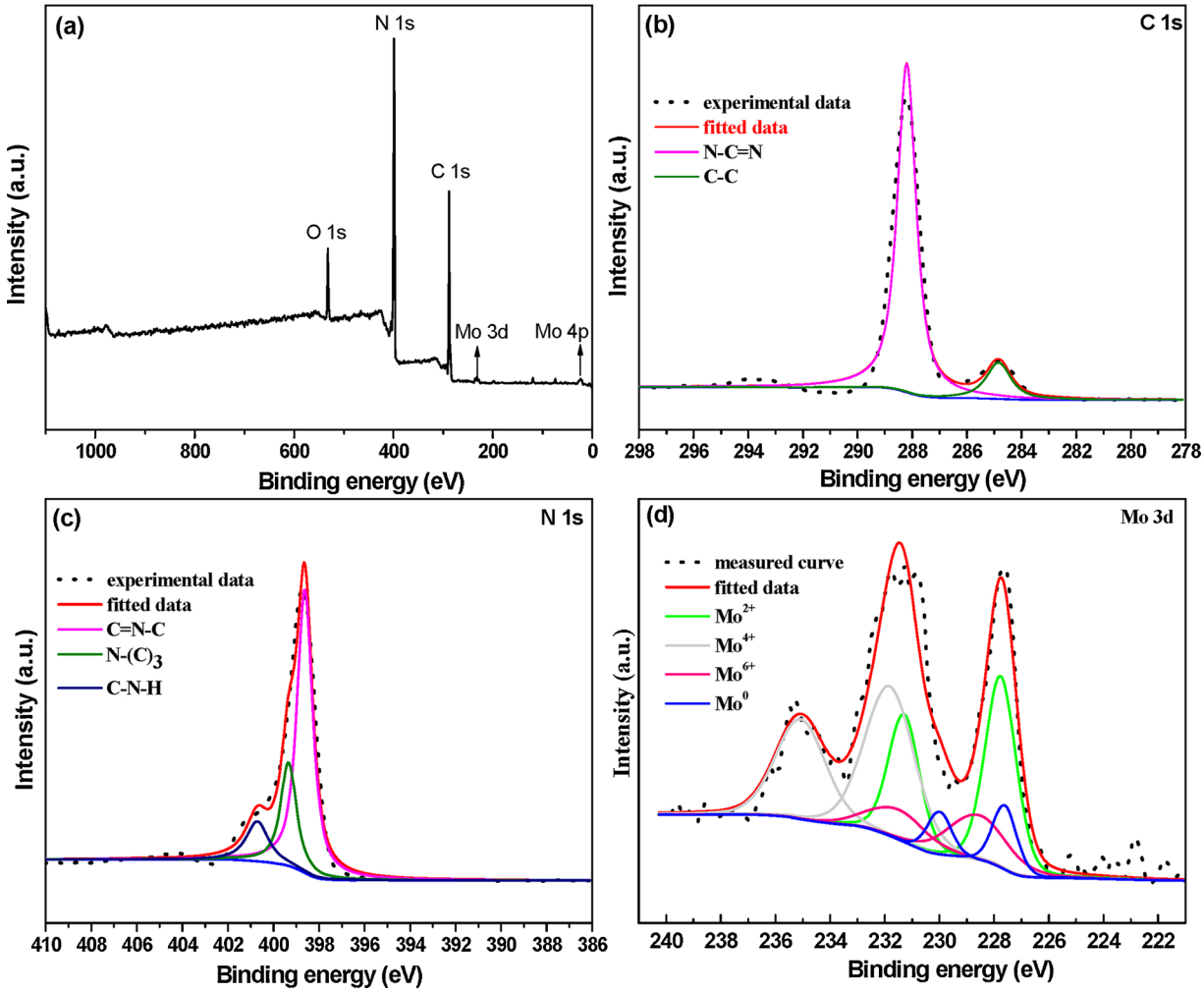

Fig. 5. XPS spectra of 2.0 wt.% Mo-Mo_2C/g-C_3N_4 photocatalyst: (a) a survey spectrum; (b) high-resolution spectra of C 1 s; (c) N 1 s and; (d) Mo 3d.

Generally, a lower PL intensity of a photocatalyst suggests that the photocatalyst has a higher charge separation efficiency for electron-hole pairs of a photocatalyst. As shown in Fig. 6(d), the intensity of the PL spectrum peak of 2.0 wt.% Mo-Mo_2C/g-C_3N_4 sample is much weaker than that of pure g-C_3N_4, indicating a higher charge separation efficiency and a lower charge recombination rate when Mo-Mo_2C cocatalyst is loaded onto the surface of g-C_3N_4 [53]. Along with the higher charge separation efficiency the enhanced visible light absorption capability also leads to a more significant photocatalytic activity increase for 2.0 wt.% Mo-Mo_2C/g-C_3N_4 photocatalyst.

3.3. Photocatalytic performance of 2.0 wt.% Mo-Mo_2C/g-C_3N_4 photocatalyst

To investigate the photocatalytic behavior of as-prepared samples were evaluated with triethanolamine (TEOA) as a sacrificial electron donor to simulate visible-light-driven hydrogen production from water. Fig. S6 show the H_2 evolution activity of Mo_2C/g-C_3N_4 photocatalysts with different loading amounts of Mo_2C. Notably, the highest photocatalytic H_2 evolution rate is achieved with 2.0 wt.% loading, which is 60.9 μmol h^{-1} $g_{catal}{}^{-1}$. Therefore, we select 2.0 wt.% Mo_2C/g-C_3N_4 photocatalyst as a reference sample. To maintain comparability, Mo-Mo_2C/g-C_3N_4 photocatalyst with a 2.0 wt.% cocatalyst concentration same to that of 2.0 wt.% Mo-Mo_2C/g-C_3N_4 was also selected as the reference sample.

Fig.7 shows the hydrogen evolution rates for six photocatalysts. Results show that pure g-C_3N_4 has a very low activity and pure Mo-Mo_2C does not have any activity at all for photocatalytic hydrogen production. When 2.0 wt.% Mo-Mo_2C cocatalyst is loaded onto the surface of g-C_3N_4 main photocatalyst, the photocatalytic activity of the g-C_3N_4 catalyst increases significantly. This result indicates that Mo-Mo_2C is an effective cocatalyst for photocatalytic H_2 production. As shown in Fig. 7, the 5-hour average hydrogen evolution rates over 2.0 wt.% Mo_2C/g-C_3N_4, 2.0 wt.% Mo/g-C_3N_4, 2.0 wt.% Mo-Mo_2C/g-C_3N_4, 0.5 wt.% Pt/g-C_3N_4 and g-C_3N_4 catalysts are 60.9, 19.1, 219.7, 244.1 and 0.5 μmol h^{-1} g^{-1}, respectively. The hydrogen evolution rate (219.7 μmol h^{-1} g^{-1}) for 2.0 wt.% Mo-Mo_2C/g-C_3N_4 photocatalyst is 440 times greater than that of g-C_3N_4 and 90% of the rate for 0.5 wt.% Pt/g-C_3N_4. The apparent quantum efficiency for hydrogen production over 2.0 wt.% Mo-Mo_2C/g-C_3N_4 was measured to be 8.3% at 420 nm light irradiation. Compared with the hydrogen evolution rate for 2.0 wt.% Mo_2C/g-C_3N_4 and 2.0 Mo wt.%/g-C_3N_4 photocatalysts, the rate for 2.0 wt.% Mo-Mo_2C/g-C_3N_4 has increased from 60.9 and 16.1 to 219.7 μmol h^{-1} g^{-1}, a 3.6 times increase over 2.0 Mo_2C/g-C_3N_4 and an 11.5 times increase over 2.0 wt.% Mo/g-C_3N_4. The significantly increased hydrogen evolution rate for the 2.0 wt.% Mo-Mo_2C/g-C_3N_4 photocatalyst results from the presence of metallic Mo in Mo_2C cocatalyst, which increases the conductivity of the cocatalyst particles. The metallic Mo particles in Mo_2C also play an important role in the electron transfer from g-C_3N_4 to combine with holes from Mo_2C to form an electron-hole pair scheme as described in the following section. It is noted that the efficiency of the 2.0 wt.% Mo-Mo_2C/g-C_3N_4 is higher than most recently reported g-C_3N_4-based photocatalysts (Table S2). Fig. 8 shows the stability for 2.0 wt.% Mo-Mo_2C/g-C_3N_4 photocatalyst

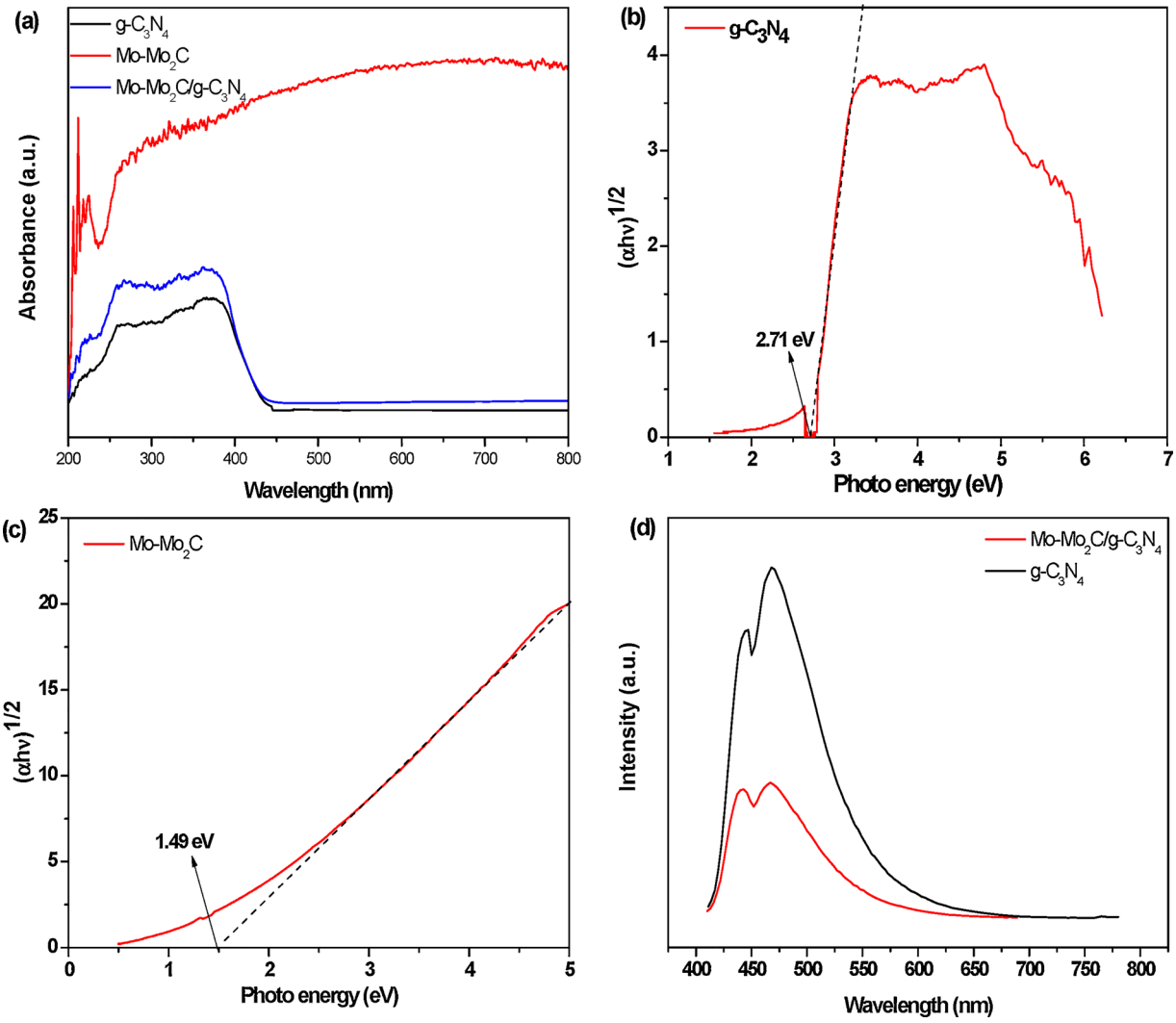

Fig. 6. (a) UV–vis diffusion reflection spectra (DRS) of g-C_3N_4, Mo-Mo_2C and 2.0 wt.% Mo-Mo_2C/g-C_3N_4. (b) $(\alpha h\nu)^{1/2}$ vs. photonic energy ($h\nu$) for g-C_3N_4. (c) $(\alpha h\nu)^{1/2}$ vs. photonic energy ($h\nu$) for Mo-Mo_2C and (d) PL spectra of g-C_3N_4 and 2.0 wt.% Mo-Mo_2C/g-C_3N_4.

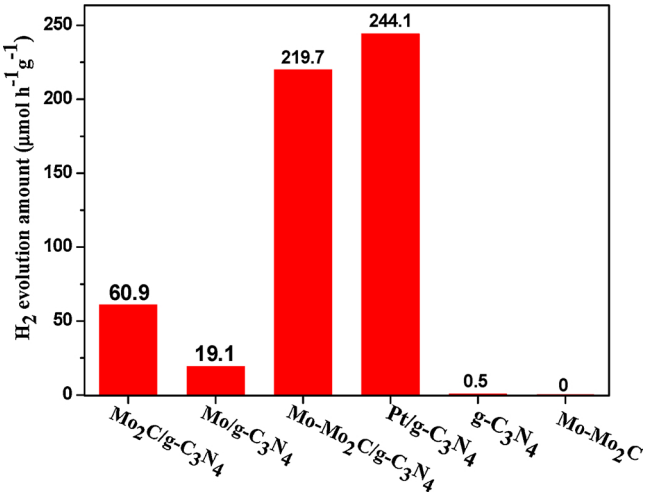

Fig. 7. Specific photocatalytic H_2 evolution rates of 2.0 wt.% Mo_2C/g-C_3N_4, 2.0 wt.% Mo/g-C_3N_4, 0.5 wt.% Pt/g-C_3N_4, 2.0 wt.% Mo-Mo_2C/g-C_3N_4 and g-C_3N_4 under visible-light irradiation.

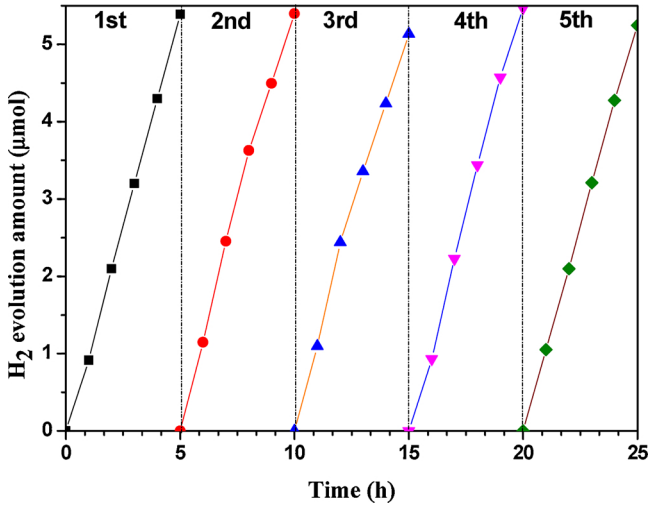

Fig. 8. Stability of H_2 evolution over 2.0 wt.% Mo-Mo_2C/g-C_3N_4 photocatalyst under visible-light irradiation.

during five consecutive hydrogen production cycles with a total of 25 h reaction time. As shown in Fig. 8, in five photocatalytic reaction cycles, the hydrogen rates of 2.0 wt.% Mo-Mo_2C/g-C_3N_4 were almost identical.

The XRD, Raman, XPS and TEM characterization for the 2.0 wt.% Mo-Mo_2C/g-C_3N_4 constructed material before and after the photocatalytic reaction were carried out. The analyses have shown that no differences in the XRD pattern (Fig. S7), Raman spectra (Fig. S8) and TEM images (Fig. 4e and Fig. S9) of the samples before and after 25 h' the H_2 evolution have been found identical. The Mo 3d XPS spectra of Mo-Mo_2C/g-C_3N_4, after a 25 h' photocatalytic reaction, is nearly the same in comparison with those before reaction (Fig. S10-S11). These observations suggest that the 2.0 wt.% Mo-Mo_2C/g-C_3N_4 photocatalyst is stable during the visible-light photocatalytic H_2 evolution reaction.

3.4. Photoelectrochemical properties of 2.0 wt.% Mo-Mo_2C/g-C_3N_4 photocatalyst

The Mo rich Mo_2C (Mo-Mo_2C) has recently been developed as an efficient electrocatalyst for HER. It exhibited a low onset potential (67 mV), a low Tafel slope (55 mV dec^{-1}) and a high exchange current density (0.019 mA cm^{-2}) for HER in an acidic medium [35]. The efficiency of a cocatalyst/photocatalyst composite is believed to be strongly influenced by the electrocatalytic performance of the cocatalyst for proton reduction [42,54]. The good electrocatalytic performance of Mo-Mo_2C is believed to contribute to the high photocatalytic activity of Mo-Mo_2C/g-C_3N_4 for H_2 production.

Fig. 9 shows the transient photocurrent responses for three photocatalyst samples: g-C_3N_4, 2.0 wt.% Mo-Mo_2C/g-C_3N_4 and 0.5 wt.% Pt/g-C_3N_4. Under dark conditions the photocurrent densities for all three samples are almost zero. Under visible light irradiation, however, the photocurrents increase significantly. The photocurrent intensity sequence of these three catalysts are: pure g-C_3N_4 < 2.0 wt.% Mo-Mo_2C/g-C_3N_4 < 0.5 wt.% Pt/g-C_3N_4. This photocurrent intensity sequence is consistent with the sequences of photocatalytic H_2 production rates.

In this research the photoelectrochemical hydrogen evolution activities of g-C_3N_4 and 2.0 wt.% Mo-Mo_2C/g-C_3N_4 were also investigated using a linear sweep voltammetry (LSV) method. In the LSV spectra the current densities of 2.0 wt.% Mo-Mo_2C/g-C_3N_4 exhibit improved performance in comparison with that of g-C_3N_4 (Fig. S12). This result indicates that Mo-Mo_2C cocatalyst is also a remarkably active photoelectrocatalyst for water reduction. Fig. S13 illustrates the Nyquist impedance plots for g-C_3N_4, 2.0 wt.% Mo-Mo_2C/g-C_3N_4 and 0.5 wt.% Pt/g-C_3N_4 photocatalysts. For comparison, the radius of the Nyquist plot of 2.0 wt.% Mo-Mo_2C/g-C_3N_4 is significantly smaller than that of g-C_3N_4, indicating that Mo-Mo_2C cocatalyst loading significantly increases the charge transfer efficiency.

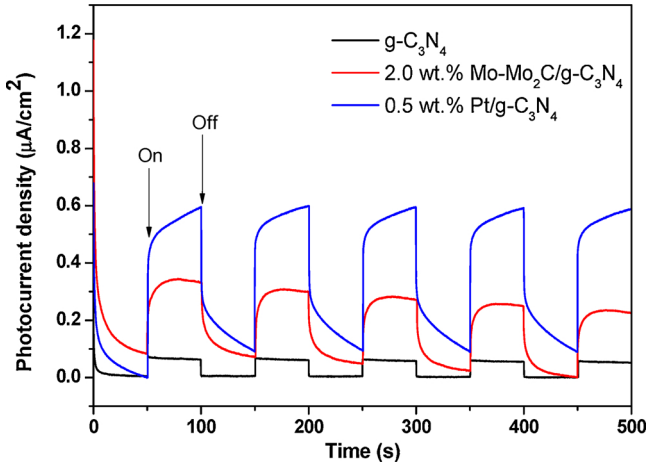

Fig. 9. Transient photocurrent responses for g-C_3N_4, 2.0 wt.% Mo-Mo_2C/g-C_3N_4 and 0.5 wt.% Pt/g-C_3N_4 photocatalysts in a 0.2 M Na_2SO_4 aqueous solution.

In summary, all the photoelectrochemical measurements and characterizations of pure g-C_3N_4, 2.0 wt.% Mo-Mo_2C/g-C_3N_4 and 0.5 wt.% Pt/g-C_3N_4 photocatalysts indicate that Mo-Mo_2C is an efficient non-noble-metal based cocatalyst for photocatalytic H_2 production.

3.5. Possible photocatalytic mechanisms of a Mo-Mo_2C/g-C_3N_4 photocatalyst

All catalyst characterization results have pointed out that the superior photocatalytic performance of a Mo-Mo_2C/g-C_3N_4 photocatalyst is attributed to the higher efficiency of charge separation and transfer of the photo-generated electron-hole pairs. In this research, Mott-Schottky (M–S) plots were carried out to determine the semiconductor types and their electronic structures for g-C_3N_4 photocatalyst and Mo-Mo_2C cocatalyst. As shown in Fig. S14, the positive slopes of M–S curves indicate that both g-C_3N_4 and Mo-Mo_2C are n-type semiconductors. The estimated flat band potentials for g-C_3N_4 and Mo-Mo_2C are -1.03 and -0.47 V vs. SCE, respectively (Fig. S14). In general, the conduction band (CB) potential of n-type semiconductors is about 0.20 V more negative than its flat band potential [55]. Thus, the CB edge potentials for g-C_3N_4 and Mo-Mo_2C are about -1.23 and -0.67 V vs. SCE, that is -0.99 and -0.43 V (vs normal hydrogen electrode (NHE)). The valence band (VB) potentials of g-C_3N_4 and Mo-Mo_2C are 1.72 and 1.06 V vs. NHE, calculated based on $E_{VB} = E_{CB} + E_g$. The electronic structures for bare Mo_2C particles were also determined using the Mott-Schottky (M–S) plot tests (Fig. S15). The calculated E_{CB} and E_{VB} edge positions of g-C_3N_4, Mo_2C and Mo-Mo_2C were summarized in Table S3.

Based on the junction of two n-type semiconductor systems of g-C_3N_4 and Mo-Mo_2C we can propose a photocatalytic mechanism to explain the improved photocatalytic efficiency of 2.0 wt.% Mo-Mo_2C/g-C_3N_4 photocatalyst for hydrogen production. Fig. 10 depicts a postulated photocatalytic mechanism. Clearly, g-C_3N_4 is a conjugated host scaffold that co-assembles with a secondary Mo_2C semiconductor. A metallic Mo particle can serve as an electron mediator to form a solid-state Z-scheme system [56–58]. As shown in Fig. 10(a), the photo-excited electrons in conduction band (CB) of g-C_3N_4 can migrate to a Mo metallic particle, where they combine holes from Mo_2C as a relay of the electron and hole pairs. The photogenerated electrons in the CB of Mo_2C (in Mo-Mo_2C) have sufficient reduction power (-0.43 V) to catalyze a proton reduction reaction for H_2 production. Simultaneously, photogenerated holes in the valance band (VB) of g-C_3N_4 can oxidize TEOA with potential of 1.72 V (vs. NHE)). This scheme of charge transfer promotes a higher H_2 production rate than can be achieved by an Mo_2C/g-C_3N_4 photocatalyst. For the Mo_2C/g-C_3N_4 composite, the band edge positions of g-C_3N_4 and Mo_2C constitute a n-n type heterojunction (Fig. 10(b)), CB-electrons of g-C_3N_4 can be inject into the CB of Mo_2C reduction active sites for participating H_2 production reaction. Meanwhile, VB-holes of g-C_3N_4 are reacted with the TEOA in the aqueous solution. Certainly, some VB-holes of g-C_3N_4 can transfer to the VB of Mo_2C and combine with electrons to accelerate charge carriers recombination. Therefore, the Mo_2C/g-C_3N_4 photocatalyst shows weakened photocatalytic H_2 production in agreement with the above theories. That is, the charge carriers separation and recombination are two competition processes. Based on these results we can conclude that Mo metal particles in the Mo-Mo_2C composite cocatalyst greatly improve the separation rate of electron-hole pairs, resulting in significant enhancement of photocatalytic activity of the Mo-Mo_2C/g-C_3N_4 photocatalyst.

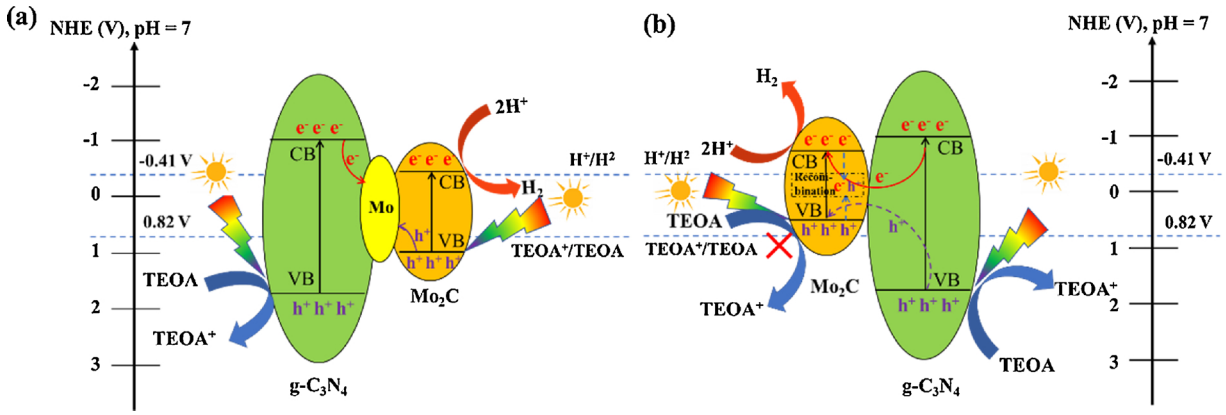

Fig. 10. Schematic diagrams of electron transfer in (a) Mo-Mo_2C/g-C_3N_4 and (b) Mo_2C/g-C_3N_4 system.

4. Conclusions

In this research we report a Mo rich Mo_2C (Mo-Mo_2C) metal/metal carbide composite as a non-noble-metal cocatalyst for efficient photocatalytic H_2 production. The Mo-Mo_2C was deposited onto the surface of g-C_3N_4 semiconductor photocatalyst for hydrogen production under visible light irradiation. The 2.0 wt.% Mo-Mo_2C/g-C_3N_4 photocatalyst was prepared using an ultrasonic-assisting deposition method. The 2.0 wt.% Mo-Mo_2C/g-C_3N_4 semiconductor/metal/ semiconductor nanocomposite photocatalyst exhibits a high H_2 production rate of 219.7 μmol h^{-1} g^{-1} with 8.3% apparent quantum efficiency, which is 440 times greater than that of g-C_3N_4 alone and 90% of that of 0.5 wt.% Pt/g-C_3N_4. It is also 3.6 times greater than that of 2.0 wt.% Mo_2C/g-C_3N_4 photocatalyst and 11.5 times greater than that of 2.0 wt.% Mo/g-C_3N_4 photocatalyst. The superior photocatalytic performance of the 2.0 wt.% Mo-Mo_2C/g-C_3N_4 photocatalyst results from fast electron transfer, which reduces the recombination of electron-hole pairs. This work reveals a new and low-cost non-noble-metal cocatalyst system for highly efficient photocatalytic solar H_2 evolution.

Acknowledgments

The National Natural Science Foundation of China (21103106, 21107069), Shanghai Key Project for Fundamental Research (13JC1402800), and Science and Technology Commission of Shanghai Municipality (14DZ2261000) support this research and are acknowledged.

Appendix A. Supplementary data

Supplementary material related to this article can be found, in the online version, at doi:https://doi.org/10.1016/j.apcatb.2018.10.016.

References

[1] C.C. Chen, W.H. Ma, J.C. Zhao, Chem. Soc. Rev. 39 (2010) 4206–4219.
[2] Y. Zheng, L. Lin, B. Wang, X. Wang, Angew. Chem. Int. Ed. Engl. 54 (2015) 12868–12884.
[3] A. Kudo, Y. Miseki, Chem. Soc. Rev. 38 (2009) 253–278.
[4] X. Wang, K. Maeda, A. Thomas, K. Takanabe, G. Xin, J.M. Carlsson, K. Domen, M. Antonietti, Nat. Mater. 8 (2009) 76–80.
[5] K. Maeda, K. Domen, J. Phys. Chem. Lett. 1 (2010) 2655–2661.
[6] K. Maeda, K. Teramura, D. Lu, T. Takata, N. Saito, Y. Inoue, K. Domen, Nature 440 (2006) 295-295.
[7] X. Zhang, L. Yu, C. Zhuang, T. Peng, R. Li, X. Li, ACS Catal. 4 (2014) 162–170.
[8] S. Cao, J. Yu, J. Phys. Chem. Lett. 5 (2014) 2101–2107.
[9] W.J. Ong, L.L. Tan, Y.H. Ng, S.T. Yong, S.P. Chai, Chem. Rev. 116 (2016) 7159–7329.
[10] X. Wang, S. Blechert, M. Antonietti, ACS Catal. 2 (2012) 1596–1606.
[11] J. Wen, J. Xie, X. Chen, X. Li, Appl. Surf. Sci. 391 (2017) 72–123.
[12] J. Liu, W. Li, L. Duan, X. Li, L. Ji, Z. Geng, K. Huang, L. Lu, L. Zhou, Z. Liu, W. Chen, L. Liu, S. Feng, Y. Zhang, Nano Lett. 15 (2015) 5137–5142.
[13] N. Liu, M. Han, Y. Sun, C. Zhu, Y. Zhou, Y. Zhang, H. Huang, V. Kremnican, Y. Liu, Y. Lifshitz, Z. Kang, Energ. Environ. Sci. 11 (2018) 1841–1847.
[14] L. Cui, X. Ding, Y. Wang, H. Shi, L. Huang, Y. Zuo, S. Kang, Appl. Surf. Sci. 391 (2017) 202–210.
[15] X.H. Li, J.S. Chen, X. Wang, J. Sun, M. Antonietti, J. Am. Chem. Soc. 133 (2011) 8074–8077.
[16] J. Liu, H.Q. Wang, Z.P. Chen, H. Moehwald, S. Fiechter, R. van de Krol, L.P. Wen, L. Jiang, M. Antonietti, Adv. Mater. 27 (2015) 712–718.
[17] J.J. Zhu, Y.C. Wei, W.K. Chen, Z. Zhao, A. Thomas, Chem. Commun. 46 (2010) 6965–6967.
[18] B. Jia, W. Zhao, L. Fan, G. Yin, Y. Cheng, F. Huang, Cata. Sci. Technol. 8 (2018) 1447–1453.
[19] J. Oh, R.J. Yoo, S.Y. Kim, Y.J. Lee, D.W. Kim, S. Park, Chem. Eur. J. 21 (2015) 6241–6246.
[20] G. Zhang, M. Zhang, X. Ye, X. Qiu, S. Lin, X. Wang, Adv. Mater. 26 (2014) 805–809.
[21] Q. Liang, Z. Li, Z.H. Huang, F. Kang, Q.H. Yang, Adv. Funct. Mater. 25 (2015) 6885–6892.
[22] G.G. Zhang, J.S. Zhang, M.W. Zhang, X.C. Wang, J. Mater. Chem. 22 (2012) 8083–8091.
[23] K. Wang, Q. Li, B.S. Liu, B. Cheng, W.K. Ho, J.G. Yu, Appl. Catal. B:Environ. 176-177 (2015) 44–52.
[24] J. Yu, K. Wang, W. Xiao, B. Cheng, Phys. Chem. Chem. Phys. 16 (2014) 11492–11501.
[25] J. Fang, H. Fan, M. Li, C. Long, J. Mater. Chem. A 3 (2015) 13819–13826.
[26] Q. Liang, Z.H. Huang, F. Kang, Q.H. Yang, ChemCatChem 7 (2015) 2897–2902.
[27] C. Ye, J.X. Li, Z.J. Li, X.B. Li, X.B. Fan, L.P. Zhang, B. Chen, C.H. Tung, L.Z. Wu, ACS Catal. 5 (2015) 6973–6979.
[28] J. He, L. Chen, Z.Q. Yi, C.T. Au, S.F. Yin, Ind. Eng. Chem. Res. 55 (2016) 8327–8333.
[29] B. Ma, H. Xu, K. Lin, J. Li, H. Zhan, W. Liu, C. Li, ChemSusChem 9 (2016) 820–824.
[30] Q.D. Yue, Y.Y. Wan, Z.J. Sun, X.J. Wu, Y.P. Yuan, P.W. Du, J. Mater. Chem. A 3 (2015) 16941–16947.
[31] Q. Xu, B. Cheng, J. Yu, G. Liu, Carbon 118 (2017) 241–249.
[32] T. Sreethawong, S. Yoshikawa, Catal. Commun. 6 (2005) 661–668.
[33] K. Shimura, H. Kawai, T. Yoshida, H. Yoshida, Chem. Commun. 47 (2011) 8958–8960.
[34] A. Iwase, H. Kato, A. Kudo, Catal. Lett. 108 (2006) 7–10.
[35] J. Dong, Q. Wu, C.P. Huang, W.F. Yao, Q.J. Xu, J. Mater. Chem. A 6 (2018) 10028–10035.
[36] D.C. Geng, X.X. Zhao, Z.X. Chen, W.W. Sun, W. Fu, J.Y. Chen, W. Liu, W. Zhou, K.P. Loh, Adv. Mater. 29 (2017) 1700072.
[37] J. Jia, W. Zhou, Z. Wei, T. Xiong, G. Li, L. Zhao, X. Zhang, H. Liu, J. Zhou, S. Chen, Nano Energy 41 (2017) 749–757.
[38] J. Gao, Z.H. Cheng, C.X. Shao, Y. Zhao, Z.P. Zhang, L.T. Qu, J. Mater. Chem. A 5 (2017) 12027–12033.
[39] Y. Li, P. Wang, C. Huang, W. Yao, Q. Wu, Q. Xu, Appl. Catal. B: Environ. 205 (2017) 489–497.
[40] J. Sun, L. Duan, Q. Wu, W. Yao, Chem. Eng. J. 332 (2018) 449–455.
[41] Q. Zhao, W. Yao, C. Huang, Q. Wu, Q. Xu, ACS Appl. Mater. Inter. 9 (2017) 42734–42741.
[42] M.H. Luo, W.F. Yao, C.P. Huang, Q. Wu, Q.J. Xu, J. Mater. Chem. A 3 (2015) 13884–13891.
[43] R. Yin, Q.Z. Luo, D.S. Wang, H.T. Sun, Y.Y. Li, X.Y. Li, J. An, J. Mater. Sci. 49 (2014) 6067–6073.
[44] Z. Li, Y. Wu, G. Lu, Appl. Catal. B: Environ. 188 (2016) 56–64.
[45] M.H. Wu, L. Li, Y.C. Xue, G. Xu, L. Tang, N. Liu, W.Y. Huang, Appl. Catal. B: Environ. 228 (2018) 103–112.
[46] B. Wang, J. Zhang, F. Huang, Appl. Surf. Sci. 391 (2017) 449–456.

[47] Q. Dong, Y. Fang, Y. Shao, P. Mulligan, J. Qiu, L. Cao, J. Huang, Science 347 (2015) 967–970.
[48] T. Komatsu, T. Nakamura, J. Mater. Chem. 11 (2001) 474–478.
[49] J. Lv, K. Dai, J.F. Zhang, L. Geng, C.H. Liang, Q.C. Liu, G.P. Zhu, C. Chen, Appl. Surf. Sci. 358 (2015) 377–384.
[50] X. Lu, Y. Jin, X. Zhang, G. Xu, D. Wang, J. Lv, Z. Zheng, Y. Wu, Dalton Trans. 45 (2016) 15406–15414.
[51] R. Tang, S. Zhou, L. Zhang, L. Yin, Adv. Funct. Mater. 28 (2018) 1706154.
[52] M. Nowak, B. Kauch, P. Szperlich, Rev. Sci. Instrum. 80 (2009) 046107.
[53] J. Zhang, L. Qi, J. Ran, J. Yu, S.Z. Qiao, Adv. Energy Mater. 4 (2014) 1301925.
[54] M.H. Luo, P. Lu, W.F. Yao, C.P. Huang, Q.J. Xu, Q. Wu, Y. Kuwahara, H. Yamashita, ACS Appl. Mater. Interfaces 8 (2016) 20667–20674.
[55] X. Li, J.G. Yu, J.X. Low, Y.P. Fang, J. Xiao, X.B. Chen, J. Mater. Chem. A 3 (2015) 2485–2534.
[56] H. Li, H. Yu, X. Quan, S. Chen, Y. Zhang, ACS Appl. Mater. Inter. 8 (2016) 2111–2119.
[57] Y. Yang, W. Guo, Y. Guo, Y. Zhao, X. Yuan, Y. Guo, J. Hazard. Mater. 271 (2014) 150–159.
[58] D. Zheng, C. Pang, X. Wang, Chem. Commun. (Camb.) 51 (2015) 17467–17470.